Current Biology *21*, 1–11, January 11, 2011 ©2011 Elsevier Ltd All rights reserved DOI 10.1016/j.cub.2010.11.056

Article

Three-Dimensional Reconstruction of Brain-wide Wiring Networks in *Drosophila* at Single-Cell Resolution

Ann-Shyn Chiang,[1,2,4,*] Chih-Yung Lin,[2,11] Chao-Chun Chuang,[5,6,11] Hsiu-Ming Chang,[1,11] Chang-Huain Hsieh,[5,11] Chang-Wei Yeh,[2,5] Chi-Tin Shih,[8,9] Jian-Jheng Wu,[8] Guo-Tzau Wang,[5] Yung-Chang Chen,[1,3] Cheng-Chi Wu,[3] Guan-Yu Chen,[3] Yu-Tai Ching,[7] Ping-Chang Lee,[7] Chih-Yang Lin,[10] Hui-Hao Lin,[2] Chia-Chou Wu,[2] Hao-Wei Hsu,[1] Yun-Ann Huang,[1] Jing-Yi Chen,[1] Hsin-Jung Chiang,[1] Chun-Fang Lu,[1] Ru-Fen Ni,[1] Chao-Yuan Yeh,[1] and Jenn-Kang Hwang[6]

[1]Brain Research Center
[2]Institute of Biotechnology
[3]Department of Electrical Engineering
National Tsing Hua University, Hsinchu 30013, Taiwan, R.O.C.
[4]Genomics Research Center, Academia Sinica, Taipei 11529, Taiwan, R.O.C.
[5]National Center for High-performance Computing, Hsinchu 30076, Taiwan, R.O.C.
[6]Institute of Bioinformatics and Systems Biology
[7]Department of Computer Science
National Chiao Tung University, Hsinchu 30010, Taiwan, R.O.C.
[8]Department of Physics, Tunghai University, Taichung 40704, Taiwan, R.O.C.
[9]Physics Division, National Center for Theoretical Sciences, Hsinchu 30043, Taiwan, R.O.C.
[10]Department of Bioinformatics, Chung Hua University, Hsinchu 30012, Taiwan, R.O.C.

Summary

Background: Animal behavior is governed by the activity of interconnected brain circuits. Comprehensive brain wiring maps are thus needed in order to formulate hypotheses about information flow and also to guide genetic manipulations aimed at understanding how genes and circuits orchestrate complex behaviors.

Results: To assemble this map, we deconstructed the adult *Drosophila* brain into approximately 16,000 single neurons and reconstructed them into a common standardized framework to produce a virtual fly brain. We have constructed a mesoscopic map and found that it consists of 41 local processing units (LPUs), six hubs, and 58 tracts covering the whole *Drosophila* brain. Despite individual local variation, the architecture of the *Drosophila* brain shows invariance for both the aggregation of local neurons (LNs) within specific LPUs and for the connectivity of projection neurons (PNs) between the same set of LPUs. An open-access image database, named FlyCircuit, has been constructed for online data archiving, mining, analysis, and three-dimensional visualization of all single neurons, brain-wide LPUs, their wiring diagrams, and neural tracts.

Conclusion: We found that the *Drosophila* brain is assembled from families of multiple LPUs and their interconnections. This provides an essential first step in the analysis of information processing within and between neurons in a complete brain.

*Correspondence: aschiang@life.nthu.edu.tw
[11]These authors contributed equally to this work

Introduction

In this age of genomics, proteomics, and metabolomics, neuroscience needs a similarly comprehensive, detailed map of brain circuits [1]. As recent advances in genetic tools for spatiotemporal control of neuronal activities have begun to unravel how genes and circuits orchestrate complex behaviors [2–4], an atlas of brain-wide wiring networks is all the more necessary for formulating hypotheses of information flow and guiding genetic manipulations [5–7]. An advantage of mapping single neurons as the basic elements is that they are well defined and easily demarcated [8, 9]. However, because of interindividual variation in synaptic arborization, a mesoscopic approach at the resolution of light microscopy is best suited for the first initial construction of brain-wide interregional connectivity maps in model systems such as the fruit fly and the mouse [1, 5, 7].

The adult *Drosophila* brain contains only ~100,000 neurons, whose projections cluster in internal neuropil structures while cell bodies are found in the outer brain surface. The *Drosophila* brain uses the canonical neurotransmitters, including acetylcholine, GABA, glutamate, dopamine, serotonin, and histamine [10–15], as well as octopamine and tyramine [16, 17]. Although clearly different in gross anatomy, both insect and mammalian brains are made of neural circuits with a cohort of shared gene products governing the normal function of sensory modalities and complex behaviors [2, 18–21]. Many common molecular mechanisms controlling development of visual and olfactory systems—which have similar circuit architecture for specific functional attributes—suggest that vertebrate and fly brains share a common evolutionary origin [22–24]. Simple brain circuits for intricate behaviors, the presence of the most sophisticated genetic toolbox, and comprehensive genomic and proteomic information make *Drosophila* an idea model system for studying basic mechanisms underlying the brain's operation [19, 25]. By integrating across different single neurons imaged at high resolution, we created a virtual fly brain assembled from information processing units and their interconnections and used it to construct a mesoscopic connectivity map.

Results

Genetic Dissection of Single Neurons

The first step in being able to assemble and integrate neurons is to orient them in the spatial coordinates of a standard model brain [26, 27]. Using genetic mosaic analysis with a repressible cell marker (MARCM) [28–33], we labeled single brain neurons born at specific times during development with green fluorescent protein (GFP) (Figure 1A). Single neurons were imaged at high resolution via an improved preparation technique [34]. Where brain images contained multiple GFP-labeled neurons, the region containing an individual neuron was semiautomatically demarcated and segmented so that each neuron could be selectively extracted from the raw image. Each segmented

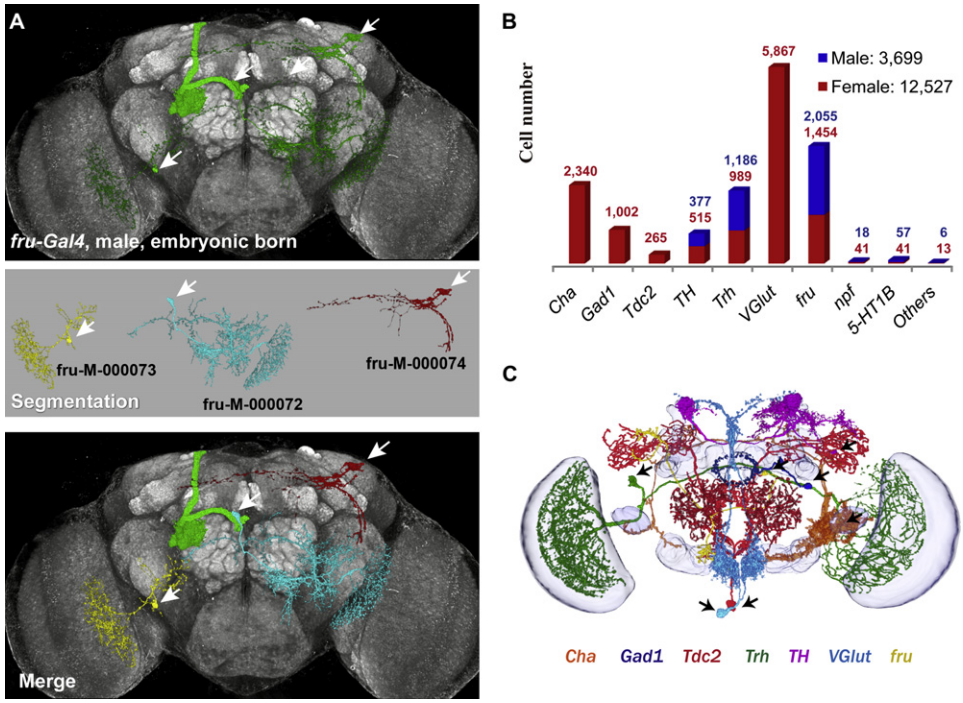

Figure 1. Large-Scale 3D Imaging and Segmentation of Single Neurons

(A) Top: a representative sample brain contains three GFP-labeled single neurons and a clone of Kenyon cells, derived from a *fru-Gal4* fly heat-shocked on day 0. Neuropils are counterstained with anti-DLG (gray). Middle: segmentation of the three single neurons. The name of each neuron is indicated. Bottom: the three "denoised" single neurons in the original sample brain.

(B) Number of single neurons collected so far. See Table S1 for number of neurons covered in each Gal4 line.

(C) A combined 3D visualization of seven different neurons, each from a separate Gal4 line, in the standard model brain. Each color represents a Gal4 line. Arrow indicates cell body.

neuron was then put back into the original sample brain, as a separate channel, so as to illustrate the clearest morphology and spatial relationships. As a starting point for a broadly representative sampling of the mesoscopic map (whose statistical reliability is confirmed below), we chose first to map neurons for the major neurotransmitter systems (Figure S1 and Table S1, available online). We have obtained high-resolution three-dimensional (3D) images of ~16,000 individual neurons, including > 10% of the total number of neurons in the adult female *Drosophila* brain (Figure 1B). An open-access database, named FlyCircuit (http://www.flycircuit.tw), has been constructed for online data archiving, mining, analysis, and 3D visualization of all the collected neurons (Figure 1C).

Generation of the Standard Model Brain

To compile single neurons taken from different flies, we generated two standard model brains representing 6-day-old *Drosophila* adults, one female (Figures 2A–2I) and one male (Figure S2A). Each standard model brain consists of average external cell cortex and inner neuropil surfaces. The template brains for registration are single male or female anti-DLG-immunostained brains that have the best fit to the average surfaces. The mushroom body (MB) of the chosen templates also has the best fit to the average MB surface in size, shape, and position (see Supplemental Experimental Procedures for the generation steps). The grayscale data of anti-DLG images used for all registrations were segmented into 58 morphologically distinguishable neuropil regions (see Figure S2B for names). All structures share a common global coordinate system whose origin is at the center of the ellipsoid body (Figure 2I).

Using the grayscale values of the anti-DLG immunostaining, each of the 16,000 sample images was registered to one of the two template brains by a global affine registration. (An affine transformation is any transformation that preserves collinearity and ratios of distances.) Our method is a nonrigid but linear registration with 12 degrees of freedom (full affine: translation, rotation, scale, and shears). Individual GFP-labeled neurons (Figure 3A) from each image were then transformed to carry them over into the space of the template brain containing confocal stacks of 58 segmented neuropil regions (Figure 3B). Each neuron's cell body was then recognized and segmented as a separate channel and its center used as the point of origin for an automated tracing of the skeleton of nerve fibers (Figure 3C). Raw data for each of the 16,000 sample images and the two template brains can be freely downloaded from the FlyCircuit website for offline analysis and evaluation of registration precision.

Cell-Type Inventory

For cross-lab validation and analysis, the registration and characterization procedures described above have been fully automated for online archiving of 3D images of single neurons (Figure S3A). Users can upload new data to compare with the existing data (see Supplemental Experimental Procedures). For each neuron, a Neuron ID page of searchable information is generated, and it includes the Gal4 driver used, putative neurotransmitter released, cell body location, and putative birth time. Although limited by the ability of light-microscopic

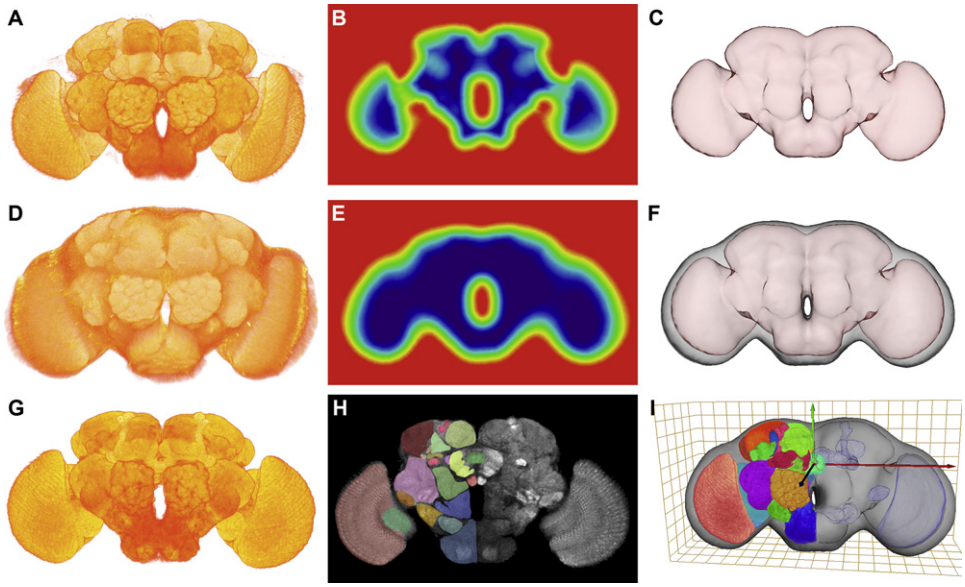

Figure 2. Steps for Making the Standard Brain Model of 6-day-old *Drosophila* Adult Females

(A) Volumetric images were acquired.

(B) A 3D signed distance map, positive (red) to negative (blue), generated from 34 samples for making the average inner brain surface.

(C) The zero crossing points determined the boundary of the averaged inner surface.

(D) Images taken with higher detection gain from the same samples used in (A).

(E) A 3D signed distance map of the outer brains.

(F) The position of the inner and outer brain was calculated.

(G) A representative brain volume was chosen to be the standard volume, with its inner surface and the position of mushroom bodies giving the best match with the average model.

(H) Neuropils in the representative brain were segmented based on anatomically distinct boundaries.

(I) A 3D coordinate was determined, originating at the geometric center of the ellipsoid body; the three axes were parallel to the principal axes of the brain with the left, anterior, and dorsal being positive.

resolution to resolve fine-grained arbors, the traced skeleton model reflects the corresponding fiber length and ensemble of terminals and, most importantly, minimizes the computational memory required for 3D visualization of a large data set (Figure S3B). The spatial distribution pattern is converted into an n-dimensional statistical distribution, where n is the total number of neuropil regions (Figure 3D). The data are then transformed into an alphabetic coding sequence, representing the number of voxels occupied by fibers innervating each of the 58 defined neuropil regions. Except for cell birth analysis, neurons used in the following analysis are all from female brains.

One caveat for the comparison of two similar neurons based on their Neuron ID is that one would be unable to distinguish sister neurons from the same neuron derived from two different flies (Figure S4A). Even if two similar neurons are derived from different Gal4 drivers, it is still impossible to distinguish whether they are two different neurons or simply the same neuron expressing both corresponding genes (Figure S4B). Occasionally, two similar neurons may be distinguishable if they are both labeled in the same sample brain.

Variability and Registration Accuracy

Because individual neurons in the fly brain are variable in size and shape (Figure S4) and sometimes even variable in their postsynaptic targets [35], it is crucial to know how the reliability of spatial relationships between neurons and brain structures are influenced by individual variability, sample preparation, and precision of computer registration and transformation. Numerous cases of repeated neurons with highly similar morphology argue that neuron-to-neuropil connections are quite consistent within different individuals. We illustrated this point with a fly expressing Gal4 in only two pairs of ventral-anterior-medial (VAM) neurons in the whole brain (Figure S4C). By repeated single-neuron imaging and quantitative measurement of innervation patterns, we found that a VAM neuron always projected its dendrites ipsilaterally to the tip of the MB α lobe and axonal terminals to the SDFP, DLP, and IDLP (Figure 4A), regardless of variations in the position of its cell body and amount of terminals (Figure 4B).

We evaluated the accuracy of brain structure alignment after image registration and transformation at three different levels: whole brain, internal neuropils, and individual neurons. Applying the automated global affine registration, sample brains and the standard model brain were highly consistent (93% ± 2% volume-to-volume ratio, n = 33). Although boundaries of internal structures may be variable after global alignment, the neuropil-to-neuropil connectivity of an individual neuron is largely preserved. For a more precise local morphological analysis, further alignment may be performed based on a selected subregion in the brain containing the structure and/or neuron of interest. Such a two-step global-local transformation procedure greatly improved the alignment accuracy of local structures. For example, the accuracy of dendritic innervations into the tip of MB α lobe from a VAM neuron was improved from 69% ± 10% (n = 10) of the original after global

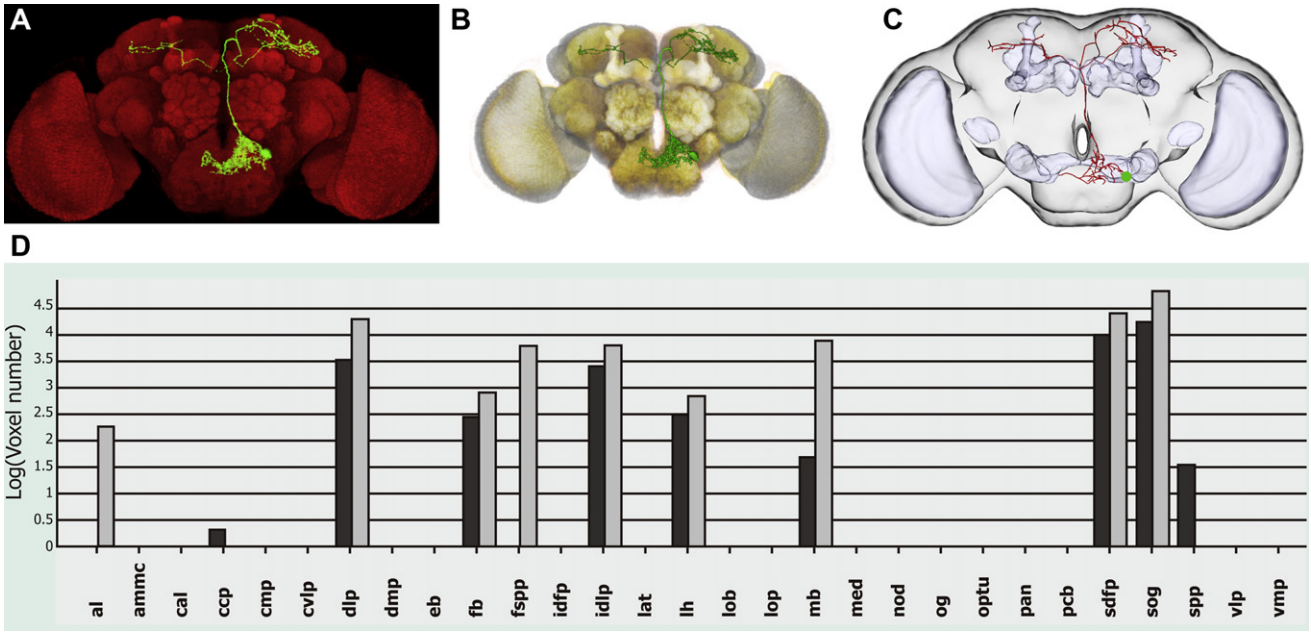

Figure 3. Automated Global Registration, Skeleton Tracing, and Spatial Distribution Analysis

(A) A sample brain (red) with a segmented single neuron (green).

(B) The neuron was carried into the standard brain (gray) through 3D registration of the sample brain (yellow).

(C) Traced neuronal skeleton in the standard model brain.

(D) Voxel distribution of the neuron in each of the 29 paired neuropil regions in the left (gray) and right (black) hemispheres. The soma was excluded.

transformation to 95% ± 3% after local transformation (Figures 4C and 4D).

Local registration can also fine-tune the alignment of internal neuropils. To evaluate the degree of registration error and variability among different brains, we calculated the distance between a landmark in each of the multiple sample brains and the standard model brain. To avoid human error in selecting the landmark, we calculated the center point of the MB vertical lobes as a landmark for each of ten sample brains used in Figure 4B. We then used the DLG-immunostained channel as a reference for the two-step global-local affine registration and calculated the distance between the landmark in each individual sample brain and the center point in the standard model brain. The average distance was 3.9 ± 0.4 μm and 1.1 ± 0.2 μm (mean ± standard error of the mean [SEM], n = 10) after global and local registration, respectively. Spatial relationships of these landmarks in the sample brains in relation to the corresponding center point in the standard model brain after local registration are given (Figure 4D). Next, using the same method, we further evaluated the registration accuracy in two additional brain regions (Figures S4D and S4E). We found that the optic glomeruli located at each side of the brain aligned less accurately than the ellipsoid body located at the center of the brain after global registration. This is as expected because uneven distortion introduced during sample preparation is inevitable and has a stronger impact on lateral structures. Nevertheless, all neuropils aligned quite well after local registration (Table S2). We noticed that, after local registration, structures with irregular shapes extending over large regions (e.g., MB) appear to align less accurately than spherical structures (e.g., EB and OG).

We used global affine registration for all FlyCircuit images as a first approximation and provide local affine registration as an option because the improved alignment from local transformation is at the expense of mismatch or distortion outside the selected region (Figure 4C).

Defining a Local Processing Unit

Brain regions are traditionally defined by anatomically distinct boundaries not necessarily representative of functional subdivisions. Neurons in the fly brain can be categorized into two functionally distinct populations: local interneurons (LNs), whose processes are restricted within a single brain region; and projection neurons (PNs), whose dendrites and axons connect between two or more brain regions. To develop a strategy for identifying basic brain building blocks, essential for analyzing network characteristics [7], we began with the well-characterized information processing unit, the antennal lobe (AL). Four classes of neurons connect in the AL: input olfactory sensory neurons, LNs, output PNs, and centrifugal neurons [36]. With a homemade semiautomated search algorithm (see "FlyCircuit/Text-based/Innervation" at http://www.flycircuit.tw), we mined all AL-LNs collected in FlyCircuit. All five previously reported categories of AL-LNs [35] were identified from FlyCircuit, even though our neurons derived from completely different sets of Gal4 lines (Figures S5A–S5C).

Results from studying the well-defined AL-LNs prompted us to examine other compartments in the fly brain where a set of LNs entangle together, even though the exact function is currently unclear. Assuming an information processing unit is equal or smaller than the boundary of an anatomically demarcated neuropil region such as the AL, we tried to detect whether a neuropil region can be further subdivided into smaller local processing units (LPUs), each containing its own population of LNs. We define a candidate LPU based on a mathematical definition of spatial features of LN branches that entangle with each other (see Supplemental Experimental Procedures). Seven steps are employed for the detection and

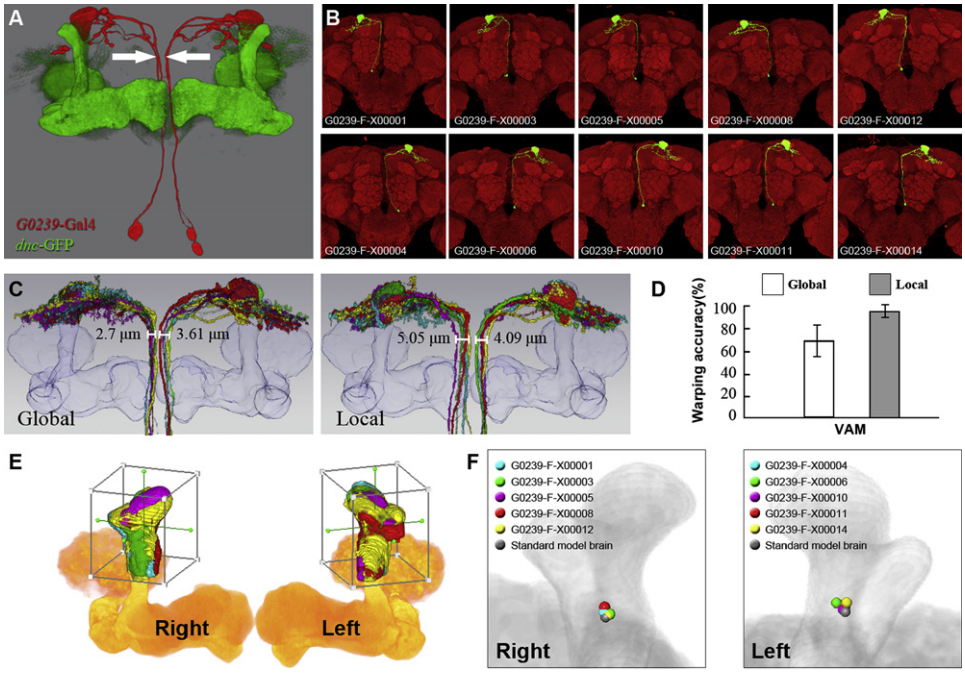

Figure 4. Brain Structure Alignment

(A) Two pairs of VAM neurons (red) innervating the tip of the α lobe of the MB (green) and the SDFP region in flies carrying the *dnc-GFP*;*G0239-GAL4*,*UAS-DsRed*;*UAS-DsRed* transgene. Their cell bodies are located in the ventral brain, and their primary neurites (arrows) project dorsally along the brain midline.
(B) Morphology and spatial distribution of VAM neurons in ten different sample brains.
(C) Registration of ten VAM neurons into the standard model brain. Alignment of VAM neurons is evaluated after a global transformation procedure by using the entire brain as a reference or after a two-step global-local transformation procedure using a part of MB vertical lobe as a reference. Whereas global transformation (left panel) considers the alignment of the entire VAM neuron, local transformation (right panel) considers only the structures within the select region (the box in E) at the expense of position reliability in other regions.
(D) Evaluation of brain structure alignment. Transformation accuracy is reflected by percentage of the volume of VAM fibers remaining in the MB lobes after transformation. Values are mean ± SEM (n = 10 for each datum).
(E) Alignment of MB vertical lobes after a two-step global-local transformation procedure. A subregion (box) of the MB vertical lobe is chosen as a reference for local transformation. Each color in the box represents a different sample aligning to the standard model (gold).
(F) Spatial distribution of landmark center points (color beads) of 10 MB vertical lobes in the sample brains in relation to the center point of the MB vertical lobe in the standard model brain.

validation of candidate LPUs: (1) calculating the number of counts passing through a voxel by populations of LNs, (2) identifying hot spots reported by the upper quartile in a five-number summary statistic [37], (3) determining subdivisions by cluster analysis, (4) recruiting LNs into each subdivision, (5) defining boundaries for each candidate LPU from LN clusters, (6) calculating the *c* value that indicates the spatial distributions of LN fibers inside each candidate LPU, and (7) validating an LPU to see whether the region has its own long-range tracts.

An operational example partitioning the ventrolateral protocerebrum (VLP) region into two LPUs is given (Figure S5D). Three criteria suggest that the dorsal and ventral VLPs may be two separate functional units: (1) each unit has its own population of LNs with segregated cell body locations, (2) neural fibers projected from the two LN clusters are segregated, and (3) each unit has its own characteristic long-range tracts communicating with different partners. Therefore, an LPU is defined as a brain region consisting of its own LN population whose nerve fibers are completely restricted to that region. Further, each LPU is contacted by at least one neural tract. In contrast, a brain region, as defined by morphologically distinct boundaries, may or may not have its own population of LNs and neural tract. Next, we applied these criteria to perform a global search for all putative LPUs.

Mapping Brain-wide Local Processing Units

Most anatomically demarcated neuropil regions, with a few exceptions, satisfied the criteria of an LPU, having segregated populations of LNs (Figure 5A). Thus far, we have identified 41 LPUs (19 paired neuropils plus three central unpaired neuropils) in the whole *Drosophila* brain (Figure 5B). Three central unpaired neuropils act as single LPUs, including the protocerebral bridge (PCB), fan-shaped body (FB), and ellipsoid body (EB). In these central unpaired LPUs, with a few exceptions, most LNs gave bilateral fibers. Detailed connectivity within the central complex will be analyzed separately. In only one case (i.e., VLP), we found two LPUs in one neuropil (Figure S5D).

Only four pairs of neuropils lack segregated populations of LNs: optic tubercle (OPTU), noduli (Nod), optic glomerulus (OG), and inner dorsolateral protocerebrum (IDLP) (Figure 5C). The OPTU is a major interhemispheric communication hub with numerous commissural fibers connecting the OPTUs in opposite hemispheres. The Nod and OG may act as information association hubs, because these two small neuropil regions contain the terminals of many PNs within the same hemisphere. Structurally, OG and Nod may be too small to accommodate extra LNs, an arrangement suggesting no further "editing" between inputs and outputs. These issues are germane to whether there is a minimum number of LNs required for forming an essential network motif [38]. The

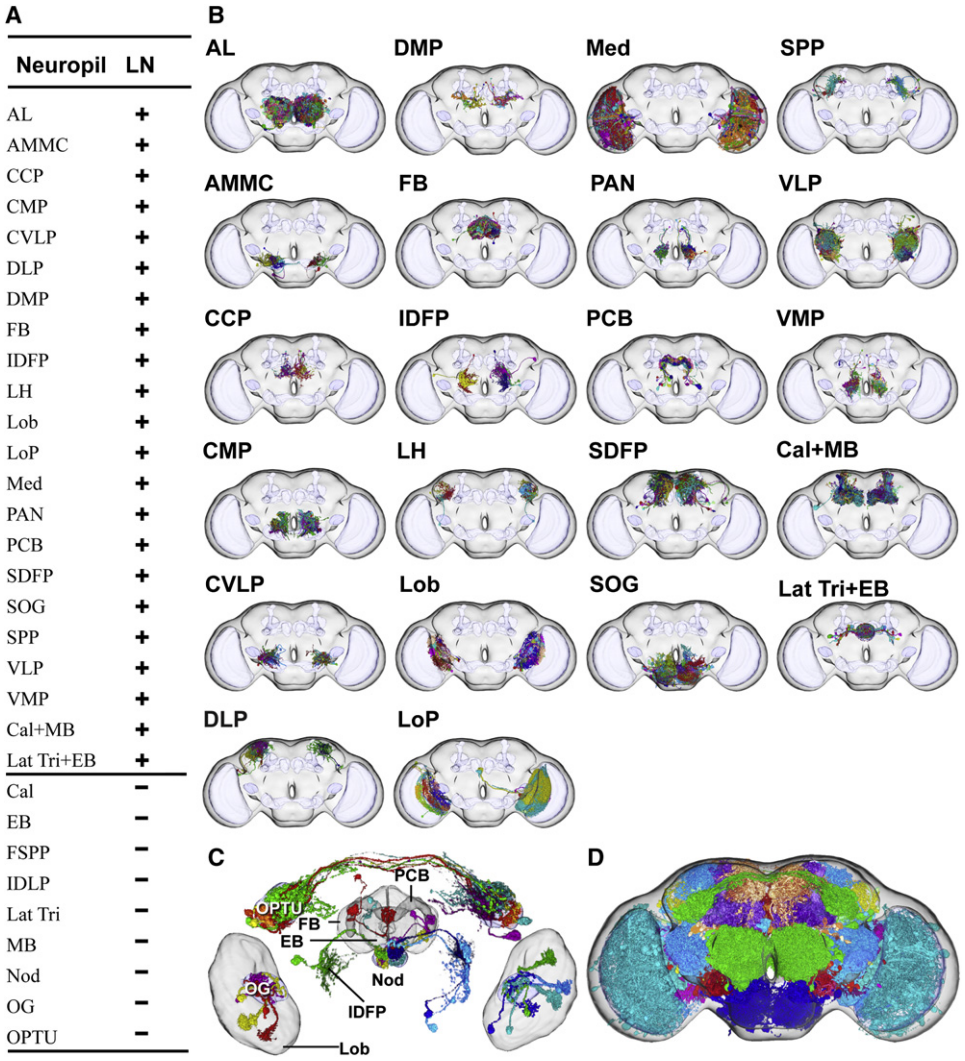

Figure 5. A Global Map of LPUs and Hubs in the Adult Female Brain

(A) Neutropils characterized by the presence (+) or absence (−) of segregated populations of LNs.

(B) Spatial distributions of putative LPUs in the standard model brain of adult females. Colors were randomly assigned to individual neurons.

(C) Spatial distribution of putative hubs lacking LNs. Paired OPTUs were linked by a segregated population of commissural PNs. Noduli were linked to PCB, FB, EB, and IDFP; OG was linked to Lob.

(D) Integration of putative LPUs and hubs fills most brain. Colors represent single neurons (B and C) or neurons in the same neuropil (D).

IDLP region has an irregular shape and an overall innervation rate of less than 30% for any neurons in FlyCircuit, suggesting that it may be an interregional path. When all of the identified LPUs and hubs are combined together, a complete brain is produced (Figure 5D). It is still possible that some LPUs may be subdivided into smaller LPUs, as in the case of dorsal and ventral VLPs (Figure S5D).

Regardless of individual variability of neurons and brain samples, the identified LPUs compiled from individual LNs were very similar to the corresponding segmented neuropils in shape and size, suggesting the coherence of our computer registration algorithm for whole-brain transformation. In total, we found ~26% of the total mapped single neurons belonging to LPU-LNs.

A Brain-wide Wiring Diagram

Complex brain networks may be quantitatively described by using graph theory as nodes (i.e., brain subdivisions) linked by directed or undirected edges (i.e., neuronal fibers) [39]. Because most LPUs coincide with neuropils that are visible in the counterstained brain samples, we first generated a pairwise connectivity matrix compiled from connection profiles between neuropils of all neurons; all LPU-LNs were excluded (Figures 6A and 6B). Hierarchical clustering of all pairwise connections revealed four families of densely interconnected LPUs coincident with specific functions (Figures 6C and 6D). Each functional module was characterized by (1) a high connection number among nodes, (2) frequent direct connections among nodes, (3) neuropils located nearby, and (4) sparse connections between nodes in different modules.

A full-scale analysis of interregional connectivity allowed us to create an undirected wiring diagram, a simplified pictorial representation of the neural circuitry of the whole *Drosophila* brain (Figure 6E). This brain-wide wiring diagram provides a global view of spatial relationships among the four identified functional modules of LPUs (Figure 6E, edge colors) and gives

information about the density of connections between 58 neuropil regions (Figure 6E, edge diameters). Sorting neurons based on their putative neurotransmitters (Table S1), we found that different functional modules tend to use different neurotransmitters (Figure 6F, Figure S6A).

One immediate and important application of the wiring diagram is to predict the higher brain centers along the circuit for a particular type of sensory information processing. For example, the antennal mechanosensory and motor center (AMMC) receives information from antennal neurons sensing environmental changes in sound, wind, and gravity, but the downstream targets of these sensory neurons remain unknown [40, 41]. Searching through FlyCircuit, we found ~400 neurons connecting the AMMC to ~28 different brain regions. Except for the highest connection density between the left and right AMMCs, about 20% of the AMMC PNs connect bilaterally to the caudal ventrolateral protocerebrum (CVLP) in both hemispheres, suggesting that CVLPs may be one of the immediate higher brain centers processing AMMC information.

Analysis of Completeness

We analyzed the spatial coverage of the expression patterns of the nine sampled Gal4 lines (Figure S1). In the entire female standard model brain, 93.03% of voxels are occupied by at least three registered neurons with few voxels uncovered (0.79%). To evaluate how often each region of the brain had been sampled, we integrated all 12,514 single neurons collected from these Gal4 lines in the female standard model brain. Most voxels registered three to 88 times (91.89%) with only a few (1.92%) unregistered. Thus, our sampling was not limited to specific brain regions and sample size is reasonably large, covering almost all brain regions. Brain-wide coverage of the sampling is most evident when a large data set is visualized (Figure 5D).

Is the connection matrix generated from ~10% of the total brain neurons representative of interregional connection patterns for the remaining 90%? To assess this, we performed a finite-size analysis comparing real data to a randomly generated network. In our network, the statistical correlation coefficient for the interregional connection matrix, presented as a function of sample size, reached more than 0.97 when the size of the randomly chosen subset of neurons was greater than 10% of our entire data set. That is, the basic pattern of the brain's connectivity is revealed with fewer than 5,000 neurons. In contrast, a random network did not reach such a high correlation until the sample size was more than 95% of the total (Figure 6G). This distinction is made clear by comparing the power-law distribution of connection numbers for the elements of the actual matrix (i.e., most neurons connect to only a few regions) to the Gaussian distribution for the randomized data (Figure 6H). Hierarchical clustering of subsets of 5,000 or 2,000 neurons also revealed that similar functional modules of densely interconnected nodes appeared in the real data, but not in the randomized connections (Figure S6B). A high correlation coefficient derived from only 10% of the collected data suggests that the 12,514 available neurons in FlyCircuit may be enough to give a good approximation of the connection patterns for the estimated ~100,000 neurons in the whole brain. Furthermore, the nine Gal4 lines used in FlyCircuit labeled more than 150,000 neurons in total (Table S1), 50% extra than the estimated total brain neurons, suggesting that these Gal4 lines may already cover most connection patterns. This, however, also indicates that these Gal4 lines are not entirely faithful in representing the endogenous expression, as expected. Further mapping of the remaining 90% of brain neurons is continuing.

A Brain-wide Map of Neural Tracts

To map the major tracts connecting different brain regions, we clustered neurons based on whether they follow a similar trajectory path linking specific LPUs. We found 58 interregional fiber bundles running along stereotyped pathways (Figure 7A). Long-range neural tracts exist for each of the four identified functional modules of LPUs and all other LPUs with unspecified functions (Figures S7A–S7E). While sensory and motor LPUs have many interhemispheric connections, other LPUs are mostly linked by association fibers connecting regions within the same hemisphere of the brain (Figures S7F and S7G).

The *Drosophila* brain consists of two symmetric hemispheres connected by numerous fibers. We found 14 commissural tracts that link an LPU or hub to its counterparts at the same level in the opposite hemisphere (Figure 7B); ten pairs of decussate tracts that obliquely cross from one hemisphere to the other (Figure 7C); and 12 pairs of associated tracts linking two LPUs in the same hemispheres (Figure 7D). The central complex develops from interhemispheric commissures (i.e., bridge-like aggregates of neurons and glia across the midline) that may share a similar origin with the corpus callosum of mammalian brains [42–44]. Analysis of numerous short-range interhemispheric connections among member elements of the central complex, presumably serving fast information exchange between the two brain hemispheres, will be addressed in the future.

Cell Birth Analysis

The adult fly brain is made of clonally related progeny from about 360 neuroblasts. Neurons of the same clonal lineage often project tightly bundled fibers along the same trajectory to innervate distinct brain areas [45], and these projections also give clues about the formation of functional modules. By sorting neurons based on their birth timing, we found that neurons linking LPUs of the locomotion module were mostly born during early larval stages. In contrast, PNs belonging to the visual and olfactory modules were born throughout the entire preadult development whereas auditory neurons were mostly born during the late larval-instar and pupal stage (Figure 8A).

Sex differences in brain structures and functions are common in all mammalian species and also occur in *Drosophila* [21, 46]. To determine whether sexual dimorphisms are also reflected in neurons' birth order, we performed a full-scale analysis of temporal changes in cell birth rate during development of each of three different types of neurons: *TH*, *Trh*, and *fru* neurons (Figure 8B; Figure S8). In contrast to the highly synchronized cell birth between sexes in both *TH* and *Trh* neurons, *fru* neurons appear to exhibit a sex-specific difference in cell birth activities. This is consistent with recent findings of large number of sexual dimorphic *fru* circuits and clones [32, 33].

Discussion

The first step toward a comprehensive analysis of information processing within and between neurons is a full map of the brain [47, 48]. Thus far, we have constructed a mesoscopic map of 41 LPUs, six hubs, and 58 tracts covering the whole

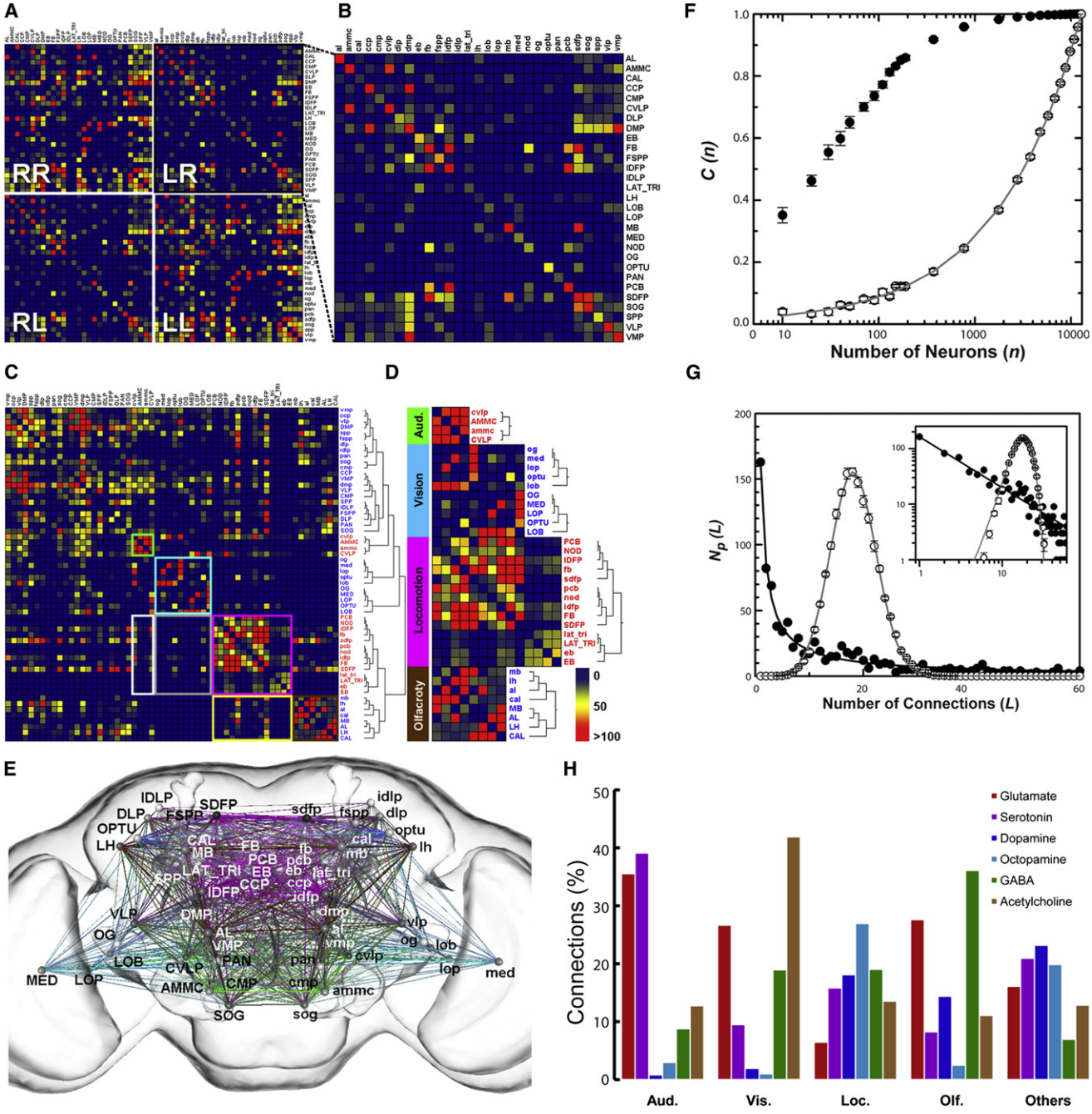

Figure 6. Brain-wide Interregional Connections

(A) The connectivity association matrix. Neuropils in the right (R, uppercase) and left (L, lowercase) hemisphere are alphabetically arranged. Each quadrant represents interconnections between neuropils in the same (RR and LL) or opposite (RL and LR) hemispheres. Connection density—the number of connections as a proportion of total number of possible connections—between two neuropils located in the same brain hemisphere was significantly higher (RR and LL) than between two neuropils in opposite hemispheres (LR and RL).

(B) An enlarged LR matrix. The number of connections is represented by colors from low (blue) to high (red). Symmetrically paired LPUs between two hemispheres of the same function were obviously interconnected.

(C) Neuropils of highest correlation are clustered.

(D) Four clustered families in C: auditory (green), visual (cyan), locomotory (pink), and olfactory (brown) networks. The white box contains nodes linking auditory and locomotory modules, the yellow box is for olfactory and locomotory, and the gray box is for visual and locomotory. The relay of connections was evaluated along paths between sensory and locomotion modules, a putative central control center. The olfactory module had more direct links than auditory and visual modules to the locomotory module.

(E) A wiring diagram indicating connections between 58 neuropils (spheres at their centers). Each functional module is indicated by a distinct color as in (D). Pure color lines are intrafunctional module connections and a mixed color indicates cross-modular connections, otherwise gray. The line thickness represents the number of connections.

(F) Connectivity patterns for real data (closed circles) and randomly generated data (open circles). The *C(n)* represents the correlation of connectivity pattern as a function of sample size *n*.

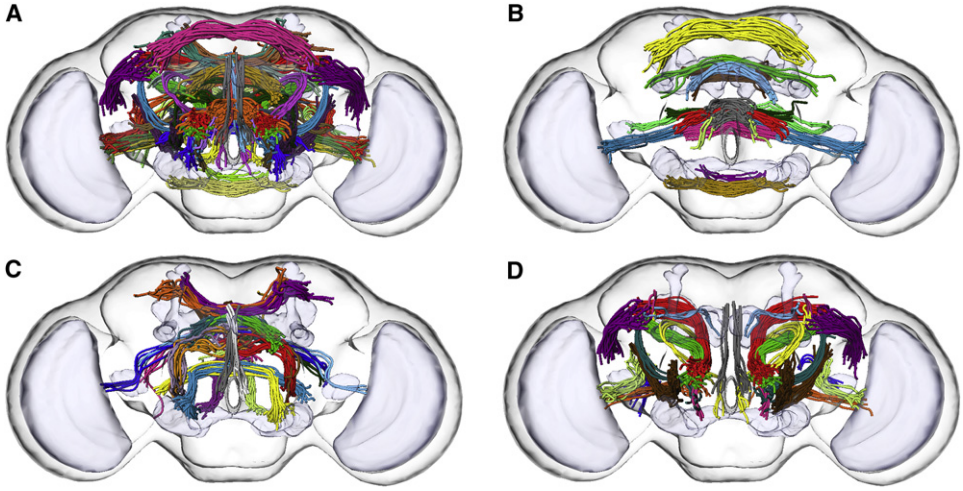

Figure 7. A Global Map of Neural Tracts

(A) An ensemble of neural tracts in the entire brain. Each color represents a distinct tract.

(B) Fourteen commissural tracts linking an LPU or a hub and its counterpart in the opposite hemisphere.

(C) Ten pairs of decussate tracts linking two different LPUs in the opposite hemispheres.

(D) Twelve pairs of association tracts linking two LPUs in the same hemispheres. Each tract is composed of at least three neurons and may actually link more than two LPUs.

Drosophila brain. Despite individual local variation, our analysis indicates that the architecture of the *Drosophila* brain shows invariant LN aggregation within specific LPUs (Figure 5) and PN connectivity between the same set of LPUs (Figure 7). Without additional details about synaptic connections, it is premature to think we can understand information processing within an LPU. On the other hand, our discovery-based FlyCircuit now permits the generation of hypotheses for predicting information flow between LPUs. In FlyCircuit, each predicted neuron in the circuit has an ID page indicating its morphology, spatial distribution, birth timing, putative neurotransmitter, source Gal4 driver, and other drivers containing similar neurons. Also, each targeted LPU has its own characteristic neural tracts. We expect that this information will be valuable for locating or generating specific intersectional drivers to manipulate the predicted circuit, using the wide range of circuit-breaking effectors available in *Drosophila*. Such a systematic description of brain architecture provides an anatomical blueprint for the accumulation of molecular and network information, eventually permitting a deep understanding of control and causality in *Drosophila* behavior.

Experimental Procedures

Transgenic Flies

Canton-S W^{1118} flies, maintained on standard cornmeal/agar/molasses medium at 25°C, were used for the generation of the standard model brains. The following transgenic fly lines were used: (1) *yw,hs-FLP/+*; FRT^{g13}, *tubP-GAL80/*FRT^{g13}*,UAS-mCD8::GFP*; *TH-GAL4/+*, (2) *hs-FLP*, FRT^{19A}*,tubP-GAL80/*FRT^{19A}, *UAS-mCD8::GFP*; *Gad1-GAL4/+*; +, (3) *hs-FLP/VGlut-GAL4*; FRT^{g13}*,tubP-GAL80/*FRT^{g13}, *UAS-mCD8::GFP*; +, (4) *hs-FLP,*FRT^{19A}*,tubP-GAL80/*FRT^{19A}*,UAS-mCD8::GFP*; *Tdc2-GAL4/+*; +, (5) *hs-FLP/+*; FRT^{g13}*,tubP-GAL80/*FRT^{g13}*,UAS-mCD8::GFP*; *Trh-GAL4/+*, (6) *hs-FLP*, FRT^{19A}*,tubP-GAL80/*FRT^{19A}*,UAS-mCD8::GFP*; *Cha-GAL4, UAS-mCD8::GFP/+*; +, (7) *yw,hs-FLP/+*; FRT^{g13}, *tubP-GAL80/*FRT^{g13}*,UAS-mCD8::GFP*; *fru-GAL4/+*, (8) *yw,hs-FLP/+*; FRT^{g13}, *tubP-GAL80/*FRT^{g13}, *UAS-mCD8::GFP*; *npf-GAL4/+*, (9) *yw,hs-FLP/+*; FRT^{g13}, *tubP-GAL80/*FRT^{g13}*,UAS-mCD8::GFP*; *5-HT1B-GAL4/+*, (10) *hs-Flp/+*; *G0239-GAL4/+*; *UAS > rCD2,Y+ > mCD8::GFP/+*, and (11) *dnc-GFP/+*; *G0239-GAL4,UAS-DsRed/+*; *UAS-DsRed/+*.

Single-Cell Labeling

We adapted a tiling heat-shock protocol in MARCM labeling to cover most neurons that were born at different times. To do so, we kept animals in a 37°C water bath for 3 to 60 min, depending on the Gal4 driver used, with 50% overlapping periods throughout the entire development from embryo to adult eclosion. For genetic FLP-out labeling, flies were heat-shocked at the adult stage. In each case, GFP expression was controlled by a specific Gal4 driver whose expression depended on stochastic removal of a *Gal80* repressor by heat-shock-induced expression of a flipase protein during mitotic recombination at cell birth. We first chose Gal4 lines driven by the promoter of an essential protein for synthesis or processing one of the following neurotransmitters: acetylcholine (*Cha-Gal4*), dopamine (*TH-Gal4*), GABA (*Gad1-Gal4*), glutamate (*VGlut-Gal4*), octopamine (*Tdc2-Gal4*), or serotonin (*Trh-Gal4*) (Figure S5). We thus labeled in each brain an individual neuron of putative birth time and neurotransmitter type. Several additional drivers were used: *fru-Gal4*, *npf-Gal4*, *5-HT1B-Gal4*, and *G0239-Gal4*. Except in the case of *G0239-Gal4* using the mosaic FLP-out labeling technique [29], all neurons were also imaged after MARCM labeling. It is important to note that a low frequency of spontaneous marking occurs with MARCM system [49]. For example, in *fru-Gal4* females, we found GFP-labeled neurons in 52.1% brains after heat-shock (n = 532 brains) and in 17.1% brains without heat-shock (n = 64 brains), respectively.

Sample Preparation

A standard protocol for sample preparation has been established so that every brain maintains its original size and shape as much as possible. To visualize the spatial relationships between the GFP neurons and brain

(G) Histogram distribution for $N_p(L)$ versus number of interregional connection L. Inset: the power law distribution of the *FlyCircuit* data set is evident in the log-log plot. The data are average of ten samples; error bars represent standard deviations.

(H) Putative neurotransmitters used by PNs involving in the four functional modules: glutamate (red), serotonin (purple), dopamine (blue), octopamine (cyan), GABA (green), and acetylcholine (brown).

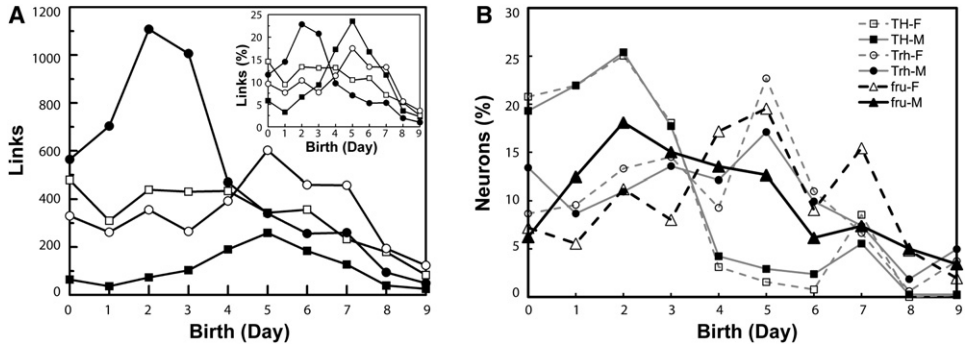

Figure 8. Birth Date Analysis

(A) Intramodular links as a function of birth timing. Inset: the ratio of links within each module.

(B) Temporal patterns of cell birth rate in three types of neurons. The birth timing for *fru* neurons shows sexual dimorphism. Coherent birth patterns are seen in *TH* and *Trh* neurons for both sexes. The number for each type of neurons analyzed is as indicated in Figure 1.

structures, we also immunostained all neuronal synapses with an antibody against the discs large (DLG) protein. Brain samples were dissected in phosphate-buffered saline (PBS) and fixed in 4% paraformaldehyde on ice with microwave irradiation (2,450 MHz, 1100 Watts) for 90 s with continuous rotation, three times. The microwave energy was measured by heating one liter of water, to be 34.98 ± 1.60 kcal (n = 6), at room temperature. After washing in PBS containing 1% Triton X-100 and 10% normal goat serum (PBS-T) for 30 min at room temperature, the brain samples were incubated in the same solution and degassed in a vacuum chamber to expel tracheal air with six cycles (depressurize to −70 mmHg then hold for 10 min). Next, the brain samples were blocked and penetrated in PBS-T at 4°C overnight and then incubated in PBS-T containing 1:50 mouse 4F3 anti-discs large monoclonal antibody (Developmental Studies Hybridoma Bank, University of Iowa) at 4°C for 2 days. After washing in PBS-T three times, the samples were incubated in PBS-T containing 1:250 biotinylated goat anti-mouse IgG (Molecular Probes) at 4°C for two days. Next, brain samples were washed and incubated with 1:500 Alexa Fluor 635 streptavidin (Molecular Probes) at 4°C overnight. Finally, after extensive washing, the immunolabeled brain samples were directly cleared in FocusClear (CelExplorer, Taiwan), an aqueous sugar-based solution rendering biological tissue transparent [50], for 5 min and then mounted in a drop of MountClear (CelExplorer) between two coverslips separated by a spacer ring of ~200 μm thickness, so the brain sample was not flattened.

Confocal Imaging

Sample brains were always imaged under a Zeiss LSM 510 confocal microscope with a 40× C-Apochromat water-immersion objective lens (N.A. value 1.2, working distance 220 μm). We imaged only brains containing one or a few nonoverlapping single neuron(s) with intense GFP labeling; others with obvious deformities, weak GFP labeling, or indistinguishable overlapping neurons were discarded. To overcome the limited field of view under high magnification, we scanned each brain in two parallel stacks of confocal images with some overlap between the two brain hemispheres. We then stitched the two image stacks into a single data set with a homemade 3D Image Stitching algorithm, using the overlapped region as a reference. The distance between successive images (z axis distance) was adjusted for the refractive index mismatch between the air and mounting medium as described previously [51]. The following settings were used in image acquisition: scanning speed 7, resolution 1024 × 1024, line average four times, zoom 0.7, and optical slice 2 μm for 20× objectives and 1 μm for 40× objectives, making the image stack composed of about 60 to 70 serial images under 20× objectives and 120 to 140 serial images under 40× objectives. The corrected voxel size of x:y:z is 0.32 × 0.32 × 1 μm.

Postrecording Image Processing

To compile all of the collected single-neuron images onto the common brain model, we first semiautomatically segmented each individual GFP-labeled neuron with Amira 4.1.2 (now Avizo, Visualization Science Group, Merignac Cedex, France). The segmented single-neuron image was then incorporated back into its originally associated background brain image, with the Zeiss LSM v.3 (Zeiss, Jena, Germany) and presented in the Neuron ID page as the original image.

Supplemental Information

Supplemental Information includes Supplemental Experimental Procedures, eight figures, and two tables and can be found with this article online at doi:10.1016/j.cub.2010.11.056.

Acknowledgments

We thank A. DiAntonio, J. Kim, B.J. Dickson, P. Shen, A. Sehgal, and T. Lee for the *VGlut-GAL4*, *Trh-GAL4*, *fru-GAL4*, *npf-GAL4*, *5-HT1B-GAL4*, and *UAS-Dscam[17.1]::GFP* fly stocks, respectively. We also thank the Bloomington Stock Center and the Drosophila Genomics Resource Center for other fly stocks and the Developmental Studies Hybridoma Bank for the 4F3 anti-discs large antibody developed by Corey Goodman. We are grateful to Josh Dubnau, Ralph Greenspan, P.C. Huang, Coby Schal, James Watson, and an anonymous referee for editorial reviews of the manuscript. This work was supported by the MOE 5-Year-50-Billion Project and NSC Nano National Project in Taiwan.

Received: October 11, 2010
Revised: November 5, 2010
Accepted: November 22, 2010
Published online: December 2, 2010

References

1. Bohland, J.W., Wu, C., Barbas, H., Bokil, H., Bota, M., Breiter, H.C., Cline, H.T., Doyle, J.C., Freed, P.J., Greenspan, R.J., et al. (2009). A proposal for a coordinated effort for the determination of brainwide neuroanatomical connectivity in model organisms at a mesoscopic scale. PLoS Comput. Biol. *5*, e1000334.
2. Olsen, S.R., and Wilson, R.I. (2008). Cracking neural circuits in a tiny brain: New approaches for understanding the neural circuitry of *Drosophila*. Trends Neurosci. *31*, 512–520.
3. Claridge-Chang, A., Roorda, R.D., Vrontou, E., Sjulson, L., Li, H., Hirsh, J., and Miesenböck, G. (2009). Writing memories with light-addressable reinforcement circuitry. Cell *139*, 405–415.
4. Krashes, M.J., DasGupta, S., Vreede, A., White, B., Armstrong, J.D., and Waddell, S. (2009). A neural circuit mechanism integrating motivational state with memory expression in *Drosophila*. Cell *139*, 416–427.
5. Kasthuri, N., and Lichtman, J.W. (2007). The rise of the 'projectome'. Nat. Methods *4*, 307–308.
6. Lichtman, J.W., and Sanes, J.R. (2008). Ome sweet ome: What can the genome tell us about the connectome? Curr. Opin. Neurobiol. *18*, 346–353.
7. Sporns, O., Tononi, G., and Kötter, R. (2005). The human connectome: A structural description of the human brain. PLoS Comput. Biol. *1*, e42.
8. Cajal, S.R. (1991). Histology of the Nervous System of Man and Vertebrates (New York: Oxford University Press).
9. Luo, L., Callaway, E.M., and Svoboda, K. (2008). Genetic dissection of neural circuits. Neuron *57*, 634–660.

10. Waddell, S. (2010). Dopamine reveals neural circuit mechanisms of fly memory. Trends Neurosci. *33*, 457–464.
11. Bicker, G. (1999). Introduction to neurotransmitter histochemistry of the insect brain. Microsc. Res. Tech. *45*, 63–64.
12. Littleton, J.T., and Ganetzky, B. (2000). Ion channels and synaptic organization: Analysis of the *Drosophila* genome. Neuron *26*, 35–43.
13. Dierick, H.A., and Greenspan, R.J. (2007). Serotonin and neuropeptide F have opposite modulatory effects on fly aggression. Nat. Genet. *39*, 678–682.
14. Budnik, V., and White, K. (1987). Genetic dissection of dopamine and serotonin synthesis in the nervous system of *Drosophila melanogaster*. J. Neurogenet. *4*, 309–314.
15. Daniels, R.W., Gelfand, M.V., Collins, C.A., and DiAntonio, A. (2008). Visualizing glutamatergic cell bodies and synapses in *Drosophila* larval and adult CNS. J. Comp. Neurol. *508*, 131–152.
16. Roeder, T. (2005). Tyramine and octopamine: Ruling behavior and metabolism. Annu. Rev. Entomol. *50*, 447–477.
17. Busch, S., Selcho, M., Ito, K., and Tanimoto, H. (2009). A map of octopaminergic neurons in the *Drosophila* brain. J. Comp. Neurol. *513*, 643–667.
18. Su, C.Y., Menuz, K., and Carlson, J.R. (2009). Olfactory perception: Receptors, cells, and circuits. Cell *139*, 45–59.
19. Simpson, J.H. (2009). Mapping and manipulating neural circuits in the fly brain. Adv. Genet. *65*, 79–143.
20. Harbison, S.T., Mackay, T.F., and Anholt, R.R. (2009). Understanding the neurogenetics of sleep: Progress from *Drosophila*. Trends Genet. *25*, 262–269.
21. Dickson, B.J. (2008). Wired for sex: The neurobiology of *Drosophila* mating decisions. Science *322*, 904–909.
22. Cajal, S., and Sánchez, D. (1915). Contribución al conocimiento de los centros nerviosos de los insectos. Trab. Lab. Inv. Biol. *13*, 1–68.
23. Sanes, J.R., and Zipursky, S.L. (2010). Design principles of insect and vertebrate visual systems. Neuron *66*, 15–36.
24. Ramdya, P., and Benton, R. (2010). Evolving olfactory systems on the fly. Trends Genet. *26*, 307–316.
25. Armstrong, J.D., and van Hemert, J.I. (2009). Towards a virtual fly brain. Philos. Transact. A Math. Phys. Eng. Sci. *367*, 2387–2397.
26. Toga, A.W. (2002). Neuroimage databases: The good, the bad and the ugly. Nat. Rev. Neurosci. *3*, 302–309.
27. Rein, K., Zöckler, M., Mader, M.T., Grübel, C., and Heisenberg, M. (2002). The *Drosophila* standard brain. Curr. Biol. *12*, 227–231.
28. Lee, T., and Luo, L. (1999). Mosaic analysis with a repressible cell marker for studies of gene function in neuronal morphogenesis. Neuron *22*, 451–461.
29. Wong, A.M., Wang, J.W., and Axel, R. (2002). Spatial representation of the glomerular map in the *Drosophila* protocerebrum. Cell *109*, 229–241.
30. Datta, S.R., Vasconcelos, M.L., Ruta, V., Luo, S., Wong, A., Demir, E., Flores, J., Balonze, K., Dickson, B.J., and Axel, R. (2008). The *Drosophila* pheromone cVA activates a sexually dimorphic neural circuit. Nature *452*, 473–477.
31. Jefferis, G.S., Potter, C.J., Chan, A.M., Marin, E.C., Rohlfing, T., Maurer, C.R., Jr., and Luo, L. (2007). Comprehensive maps of *Drosophila* higher olfactory centers: Spatially segregated fruit and pheromone representation. Cell *128*, 1187–1203.
32. Yu, J.Y., Kanai, M.I., Demir, E., Jefferis, G.S., and Dickson, B.J. (2010). Cellular organization of the neural circuit that drives *Drosophila* courtship behavior. Curr. Biol. *20*, 1602–1614.
33. Cachero, S., Ostrovsky, A.D., Yu, J.Y., Dickson, B.J., and Jefferis, G.S. (2010). Sexual dimorphism in the fly brain. Curr. Biol. *20*, 1589–1601.
34. Lin, H.H., Lai, J.S., Chin, A.L., Chen, Y.C., and Chiang, A.S. (2007). A map of olfactory representation in the *Drosophila* mushroom body. Cell *128*, 1205–1217.
35. Chou, Y.H., Spletter, M.L., Yaksi, E., Leong, J.C., Wilson, R.I., and Luo, L. (2010). Diversity and wiring variability of olfactory local interneurons in the *Drosophila* antennal lobe. Nat. Neurosci. *13*, 439–449.
36. Vosshall, L.B., and Stocker, R.F. (2007). Molecular architecture of smell and taste in *Drosophila*. Annu. Rev. Neurosci. *30*, 505–533.
37. Hoaglin, D.C., Mosteller, F., and Tukey, J.W. (1983). Understanding Robust and Exploratory Data Analysis (New York, Chichester: Wiley).
38. Milo, R., Shen-Orr, S., Itzkovitz, S., Kashtan, N., Chklovskii, D., and Alon, U. (2002). Network motifs: Simple building blocks of complex networks. Science *298*, 824–827.
39. Bullmore, E., and Sporns, O. (2009). Complex brain networks: Graph theoretical analysis of structural and functional systems. Nat. Rev. Neurosci. *10*, 186–198.
40. Yorozu, S., Wong, A., Fischer, B.J., Dankert, H., Kernan, M.J., Kamikouchi, A., Ito, K., and Anderson, D.J. (2009). Distinct sensory representations of wind and near-field sound in the *Drosophila* brain. Nature *458*, 201–205.
41. Kamikouchi, A., Inagaki, H.K., Effertz, T., Hendrich, O., Fiala, A., Göpfert, M.C., and Ito, K. (2009). The neural basis of *Drosophila* gravity-sensing and hearing. Nature *458*, 165–171.
42. Hanesch, U.F., Fischbach, K.-F., and Heisenberg, M. (1989). Neuronal architecture of the central complex in *Drosophila melanogaster*. Cell Tissue Res. *257*, 343–366.
43. Silver, J., Lorenz, S.E., Wahlsten, D., and Coughlin, J. (1982). Axonal guidance during development of the great cerebral commissures: Descriptive and experimental studies, in vivo, on the role of preformed glial pathways. J. Comp. Neurol. *210*, 10–29.
44. Therianos, S., Leuzinger, S., Hirth, F., Goodman, C.S., and Reichert, H. (1995). Embryonic development of the *Drosophila* brain: Formation of commissural and descending pathways. Development *121*, 3849–3860.
45. Ito, K., and Awasaki, T. (2008). Clonal unit architecture of the adult fly brain. Adv. Exp. Med. Biol. *628*, 137–158.
46. Jazin, E., and Cahill, L. (2010). Sex differences in molecular neuroscience: From fruit flies to humans. Nat. Rev. Neurosci. *11*, 9–17.
47. Geschwind, D.H., and Konopka, G. (2009). Neuroscience in the era of functional genomics and systems biology. Nature *461*, 908–915.
48. Arenkiel, B.R., and Ehlers, M.D. (2009). Molecular genetics and imaging technologies for circuit-based neuroanatomy. Nature *461*, 900–907.
49. Fox, D.T., and Spradling, A.C. (2009). The *Drosophila* hindgut lacks constitutively active adult stem cells but proliferates in response to tissue damage. Cell Stem Cell *5*, 290–297.
50. Chiang, A.S., Liu, Y.C., Chiu, S.L., Hu, S.H., Huang, C.Y., and Hsieh, C.H. (2001). Three-dimensional mapping of brain neuropils in the cockroach, *Diploptera punctata*. J. Comp. Neurol. *440*, 1–11.
51. Liu, Y.C., and Chiang, A.S. (2003). High-resolution confocal imaging and three-dimensional rendering. Methods *30*, 86–93.